RMetS
Royal Meteorological Society

Decision theory-based detection of atmospheric natural hazards from satellite imagery using the example of volcanic ash

L. M. Western,[a]* J. Rougier[b] and I. M. Watson[a]
[a]*School of Earth Sciences, University of Bristol, UK*
[b]*School of Mathematics, University of Bristol, UK*

*Correspondence to: L. M. Western, School of Earth Sciences, Wills Memorial Building, Queen's Road, Bristol BS8 1RJ, UK.
E-mail: luke.western@bristol.ac.uk

Atmospheric natural hazards pose a risk to people, aircraft and infrastructure. Automated algorithms can detect these hazards from satellite imagery so that the relevant advice can be issued. The transparency and adaptability of these automated algorithms is important to cater to the needs of the end user, who should be able to readily interpret the hazard warning. This means avoiding heuristic techniques. Decision theory is a statistical tool that transparently considers the risk of false positives and negatives when detecting the hazard. By assigning losses to incorrect actions, ownership of the hazard warning is shared between the scientists and risk managers. These losses are readily adaptable depending on the perceived threat of the hazard. This study demonstrates how decision theory can be applied to the detection of atmospheric natural hazards using the example of volcanic ash during an ongoing eruption. The only observations are the difference in brightness temperature between two channels on the SEVIRI sensor. We apply the method to two volcanic eruptions: the 2010 eruption of Eyjafjallajökull, Iceland, and the 2011 eruption of Puyehue-Cordón Caulle, Chile. The simple probabilistic method appears to work well and is able to distinguish volcanic ash from desert dust, which is a common false positive for volcanic ash. As is made clear, decision theory is a tool for decision support, providing transparency and adaptability, but it still requires careful input from scientists and risk managers. Effectively it provides a space where these groups of experts can meet and convert their shared understanding of a hazard into a choice of action.

Key Words: detection of atmospheric natural hazards; weather risk; uncertainty in Earth observation; decision support

Received 09 June 2017; Revised 12 December 2017; Accepted 14 December 2017; Published online in Wiley Online Library

1. Introduction

Weather hazards are the main cause for delays in air traffic and contribute to around 20% of aviation accidents (Mecikalski *et al.*, 2007). It is important to detect and track these hazards as reliably as possible so that the relevant authorities can issue accurate and timely advice. This requires constant monitoring of the Earth's atmosphere, which is possible using sensors found on board satellites. These satellite measurements inform experts, who identify the hazard and track it over its lifetime. This expert judgment then informs risk managers, who are responsible for issuing the warning. However, there is a growing demand for the automation of hazard warning systems (Bhattacharya *et al.*, 2012). The problem is that human judgement is difficult to replicate. Humans have an aptitude for pattern recognition, which scientists attempt to replicate through advanced hazard detection schemes. These detection schemes are often heuristic and specific to an instrument and organization, such as some measurement exceeding a threshold value. The consequences of a hazard warning differ for those issuing and those receiving it. This means that a hazard warning is never a true or false, only good or bad (Rittel and Webber, 1973). A hazard warning issuing a false alarm is perceived as bad if the reason for the false alarm is not understood (Dow and Cutter, 1998). This means that any automated hazard warning system should be as transparent as possible, where scientists share ownership with risk managers on what they perceive makes a good warning. As a result, an automated warning system should avoid heuristics, instead dealing with uncertainties transparently, where the perceived loss in issuing an incorrect warning is readily accessible. A framework that allows this is decision theory.

This study outlines how decision theory can be applied to remote sensing of atmospheric natural hazards. By using the example of detecting volcanic ash hazards, this study demonstrates

Table 1. Example of a loss table.

$L(a,x)$	x_1	x_2	$\cdots$	x_n
$a=a_1$	ℓ_{11}	ℓ_{12}	$\cdots$	ℓ_{1n}
$a=a_2$	ℓ_{21}	ℓ_{22}	$\cdots$	ℓ_{2n}
$\vdots$	$\vdots$	$\vdots$	$\ddots$	
$a=a_m$	ℓ_{m1}	ℓ_{m2}		ℓ_{mn}

how decision theory can be used to classify the atmosphere as uncontaminated or contaminated using the reverse absorption technique (section 3.1) and the Spinning Enhanced Visible and Infrared Imager (SEVIRI) (section 3.2). Section 2 gives an outline to decision theory and applies it to the detection of volcanic ash in section 3. Two examples demonstrate the methodology, the 2010 eruption of Eyjafjallajökull and the 2011 eruption of Puyehue-Cordón Caulle, in section 4. Section 5 discusses and section 6 concludes the findings of the study.

2. Decision theory

Decision theory aims to make a 'good' decision about which action to take. Some set of actions $a \in \mathcal{A}$ describe the atmosphere based on a set of exclusive and exhaustive states $x \in X$. The probability of the atmosphere being in a certain state depends on the observation y. Bayes's theorem describes the probability that the atmosphere is in state x given the observation y by

$$P(x \mid y) = \frac{P(y \mid x)P(x)}{P(y)}. \tag{1}$$

A decision based on the most probable state ignores the loss in taking the wrong action. This is not a rational decision; a rational decision is to take the action with the lowest associated risk. This is the basis of decision theory – a framework that includes the losses associated with each possible action in the decision-making process. For this a loss must be attributed to each action for each state of nature. A loss table, similar to Table 1, summarizes the losses represented by the loss function $L(a,x)$.

These losses could be individually specified by a risk manager, or using some low-dimensional parametrization of the loss function (e.g. Economou *et al.*, 2016). Many forms of loss exist, such as the loss of profit, loss due to regret, loss of reputation or loss of life, amongst others. The losses can be both positive and negative, where a negative loss indicates gain (e.g. DeGroot, 1970; Lindley, 1985). This study deals with only non-negative losses. Although this implies that there is never a gain in making a correct decision, it is satisfactory that there is no loss in making a correct decision.

Losses differ depending on the stakes of the decision, which differ between users. For a multiple step procedure, an initial, computationally cheap test with high sensitivity at the cost of specificity could provide the input for a more computationally expensive test where the sensitivity and specificity are more equally weighted. Here the preference to sensitivity and specificity in the procedure are controlled transparently by the losses provided. Risk managers should assign losses which are as representative as possible of human rational decision making, much as scientists attempt to automate human-like expertise. However, small changes in the losses or posterior probability are unlikely to change the optimal action (Degroot, 1970).

In Bayesian decision theory, the optimal action based on the observations minimizes the expected loss over all actions, conditional on the observations. Thus for observations y the Bayes action is

$$a^*(y) = \underset{a\in\mathcal{A}}{\arg\min} \sum_x L(a,x)\, P(y \mid x)\, P(x), \tag{2}$$

applying Bayes's theorem, and neglecting the denominator, which does not depend on a. The summation in Eq. (2) becomes an integral for continuous x. DeGroot (1970) gives more details.

3. Using decision theory to detect volcanic ash hazards with the SEVIRI sensor

Decision theory can be straightforwardly applied to remote detection of volcanic ash. Volcanic ash poses a threat to aircraft, amongst other things, and there is a loss in falsely classifying a pixel that contains as ash free. There is also a loss if a pixel is classified as containing ash when there is none, as this could lead to unnecessary closure of airspace. This section presents a method using decision theory to classify each pixel from a SEVIRI image as uncontaminated or contaminated, depending on whether volcanic ash is absent or present in the pixel. The classification of airspace as uncontaminated or contaminated based only on remote-sensing observations of volcanic ash is an overly simplistic approach to volcanic ash hazard mitigation. However, it demonstrates the nature and potential of applying decision theory to the detection of atmospheric natural hazards.

3.1. Remote sensing of volcanic ash

A simple, common test for volcanic ash using infrared satellite observations is the reverse absorption technique (Prata, 1989a, 1989b). This technique relies on the difference in brightness temperature between channels centred around 11 and 12 μm being, in general, negative for volcanic ash clouds and positive for water and ice clouds, and is used for the observation y. Although more robust methods of ash detection exist, the reverse absorption technique allows for a simple demonstration of where uncertainty arises from observation (Simpson *et al.*, 2000; Prata *et al.*, 2001). The underlying surface type, ambient meteorological conditions and properties of the volcanic ash cloud can all contribute to uncertainty in the detection. For example, high water vapour may obscure the reverse absorption feature, especially for low-altitude volcanic clouds. This uncertainty not only occurs for detection methods that use heuristic thresholds, but also for probabilistic methods where the likelihood space can overlap (Pavolonis *et al.*, 2015a). A common false positive for volcanic ash is desert dust, which also exhibits this reverse absorption feature (Ackerman, 1997). As a result there is no universal threshold between ash and ash-free conditions.

3.2. Observations using SEVIRI

This study uses radiances measured by SEVIRI on board the geostationary Meteosat Second Generation (MSG) satellites located at 0° longitude (Aminou, 2002). SEVIRI has a 3 km nadir pixel resolution at the wavelengths of interest, which increase in size with zenith angle, and has a baseline repeat cycle of 15 min. The observation uses the brightness temperature difference of two channels centred around 10.8 μm and 12.0 μm, $y = BT_{10.8\mu\mathrm{m}} - BT_{12.0\mu\mathrm{m}}$.

3.3. States, actions and losses

In this subsection, we drop the i subscript indicating the pixel to reduce clutter. We consider each satellite pixel to have one of three possible states: volcanic ash, desert dust or free from both volcanic ash and desert dust, $X_i \in \{\text{ash, dust, free}\}$ for pixel i. We assume that these three states are exclusive, e.g. a pixel cannot contain both volcanic ash and desert dust, and exhaustive, i.e. no other states exist. There is no difficulty in generalizing to allow more states, including combinations, if the application requires it. The possible set of actions is to flag the satellite pixel as contaminated, i.e. containing ash, or uncontaminated, i.e. not containing ash, $\mathcal{A} = \{\text{contaminated, uncontaminated}\}$. The loss table (Table 2) summarizes the states, actions and their losses. There is a a zero loss if the correct action is taken for a given state, i.e. $\ell_{11} = \ell_{22} = \ell_{23} = 0$. A loss occurs if the incorrect action is taken, which depends on the severity of the incorrect action. It is

Table 2. Loss table showing states, actions and losses.

$L(a,x)$	ash	dust	free
a = contaminated	ℓ_{11}	ℓ_{12}	ℓ_{13}
a = uncontaminated	ℓ_{21}	ℓ_{22}	ℓ_{23}

worth noting that the relative losses are important for deciding the optimal action, rather than the absolute losses.

3.4. *Probability density functions*

Each term in Eq. (1) needs a probability density function. Section 3.4.1 describes the likelihoods $P(y_i \mid x_i)$, which were fitted to past observations using an Epanechnikov kernel density estimator (Epanechnikov, 1969). Section 3.4.2 describes the prior probabilities for each state, $P(x_i)$.

3.4.1. *Likelihood of observation*

The probability density function $P(y \mid \text{ash})$ describes the probability of the observation y given an ash-filled pixel. There are two separate $P(y \mid \text{ash})$ for observations over land and sea as surface type is a first-order control on the observation y. The training set for $P(y \mid \text{ash})$ was fitted to observations using the detection method proposed in Francis *et al.* (2012) for a selection of scenes during the 2010 Eyjafjallajökull eruption (WMO, 2016). Using this training set and the technique proposed in this study, ash was detected from all available SEVIRI imagery during the 2010 Eyjafjallajökull eruption to form new $P(y \mid \text{ash})$ for land and sea. In an attempt to remove noisy pixels misidentified as ash, and to include missed pixels, a fast Fourier transform filter was applied to filter the image in the frequency domain (Appendix). Figure 1 shows $P(y \mid \text{ash})$, which was fitted to a total of 1 860 860 observed pixels over land and 8 932 287 observed pixels over sea. A training set based on a single eruption is unlikely to capture a global representation of the spectral signature of volcanic ash, but is adequate for this study. An operational detection scheme could improve its $P(y \mid \text{ash})$ by using a range of volcanic ash characteristics to form a global $P(y \mid \text{ash})$. It could also separate $P(y \mid \text{ash})$ into different states based on meteorological conditions or type of ash cloud, e.g. composition or size.

The training set for dust was the same as volcanic ash due to their similar spectral properties. Observations during large dust storms on 1 April 2015 over Arabia and 5–8 April 2011 from the Sahara, sweeping across the Atlantic Ocean up to the United Kingdom, formed $P(y \mid \text{dust})$ over both land and sea. The same fast Fourier transform filter applied to volcanic ash was applied to desert dust. Arid surfaces can also have a negative brightness temperature difference between ~11 and 12 μm (Prata *et al.*, 2001). As a result, it is highly likely that many false positives were recorded. A dust-filled state perhaps better describes a state of either airborne dust or a dusty surface, so not strictly an atmospheric state. Figure 1 shows $P(y \mid \text{dust})$, which was fitted to a total of 19 004 259 observed pixels over land and 3 039 542 observed pixels over sea.

The probability density function $P(y \mid \text{free})$ describes the probability of the observation y given a pixel free from ash and dust. Given the availability of data for pixels free from ash and dust, it is simple to construct spatially varying probability density functions, to allow for the effect of features such as longitude and latitude. Firstly, the SEVIRI field of view within 80°N, 80°E, 80°S, 80°W was divided into subregions of 20° longitude by 5° latitude. Then for each calendar month, for each subregion, there is a separate $P(y \mid \text{free})$ for land and sea. Each $P(y \mid \text{free})$ was fitted to data for y from 4 months of SEVIRI observations, using months that had no volcanic ash events or exceptionally large dust storms within the SEVIRI field of view. In areas where dust events are common, e.g. the Sahara, it is likely that many small dust events have been captured in $P(y \mid \text{free})$, in a similar way that $P(y \mid \text{dust})$ may include dusty surfaces. As the application of this study is the detection of volcanic ash, it is unlikely that this will cause problems for optimal decision-making in areas with a high number of dust events. Figure 1 shows examples of $P(y \mid \text{free})$ for April over (a) sea for the subregion 10–15°N and 40–20°E and (b) land for the subregion 35–30°S and 20–40°W.

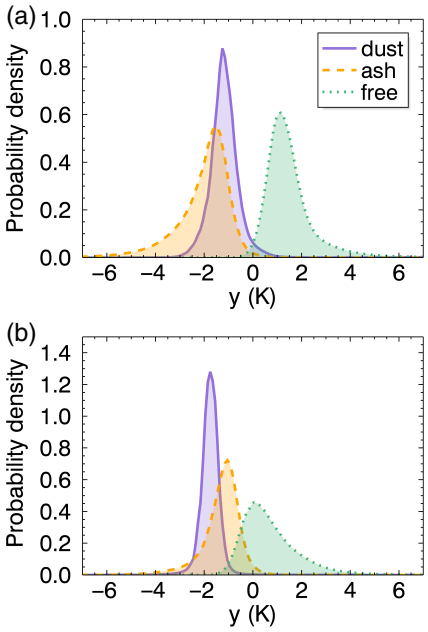

Figure 1. Examples of $P(y \mid x_j)$ for an atmospheric state containing volcanic ash, containing desert dust, and free from volcanic ash and desert dust over (a) sea and (b) land. The volcanic ash and desert dust-free states are for the subregion (a) 10–15°N and 40–20°E and (b) 35–30°S and 20–40°W. [Colour figure can be viewed at wileyonlinelibrary.com].

3.4.2. *Prior probability*

As this approach is Bayesian, each state needs its associated prior probability. The prior probability of each atmospheric state is difficult to quantify. This is especially true for volcanic ash clouds, which are infrequent and non-periodic. We therefore make the simplifying assumption that at most one volcano is erupting at any one time, so that eruptions E_j are mutually exclusive (this can be generalized if required). This prior probability is based on information available at time t, including observations from past satellite images and other sources of information, which will include whether volcano j has erupted. At a location where no information is available, there may be a general prior probability of an ash cloud (as e.g. Mackie and Watson, 2014; Pavolonis *et al.*, 2015a). Once information becomes available that an ash cloud has been detected, the prior probability of detecting ash will change. In Europe it is most likely known that an ash-bearing eruption is happening. The use of satellite remote sensing is then in response to, rather than diagnostic of, an eruption occurring. The pixel at location s_i can contain ash at time t only if a volcano has previously erupted at time t_j, and if ash has had time to travel from that volcano to location s_i. A simple model imposes a radial constant wind field from the volcano, so that the time needed for ash to travel from an eruption at the volcano E_j to pixel s_i is $d_j(s_i)/v_j$, where $d_j(s_i)$ is the great-circle distance in kilometres from volcano j to pixel s_i and v_t is the average wind velocity. The prior probability of volcanic ash is then

$$\mathrm{P}_t(x_i = \text{ash}) = \begin{cases} 0 & t - t_j < \dfrac{d_j(s_i)}{v_j}, \\ \min\left\{1, \dfrac{1}{d_j(s_i)}\right\} & t - t_j \geq \dfrac{d_j(s_i)}{v_j}. \end{cases} \quad (3)$$

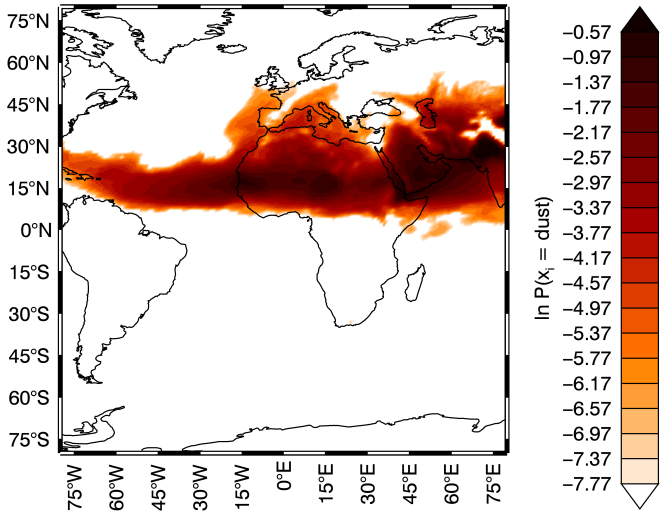

Figure 2. The prior probability of dust within the SEVIRI field of view for the month of June. [Colour figure can be viewed at wileyonlinelibrary.com].

This model could easily be generalized to use ensemble methods based on computer simulation, which is expanded upon in section 5.1.

Operationally, ensemble forecasts and any additional information could again form the prior probability for dust (e.g. Sessions *et al.*, 2015). In this study we have formed a simple prior probability for dust for each calendar month using data from the ECMWF MACC-Reanalysis dataset over a 10 year period (Inness *et al.*, 2013). At location s_i, the prior probability for dust is the proportion of 3 h intervals over the 10 year period that had a 550 nm optical depth greater than 0.5 in that location, which corresponds to a mass column loading of around 0.15 g m^{-2} (Linke *et al.*, 2006). Where there were no events in the past 10 years, we assume that P_t (x_i = dust) occurs as a 1-in-100 year event. This value represents a sufficiently unlikely event, although is not impossible. Figure 2 shows P_t (x_i = dust) for June.

In order to impose the simplifying assumption that ash, dust, and free from ash and dust are mutually exclusive and exhaustive, we combine the probabilities above as

$$P_t\,(x_i = \text{dust}) = \min\left\{P_t(x_i = \text{dust})\,,\, 1 - P_t(x_i = \text{ash})\right\}$$

and

$$P_t(x_i = \text{free}) = \max\left\{0, 1 - P_t(x_i = \text{ash}) - P_t(x_i = \text{dust})\right\}.$$

4. Examples

This section applies decision theory to the detection of ash hazards, using the reverse absorption technique and the SEVIRI sensor, to two examples: the 2010 eruption of Eyjafjallajökull, Iceland and the 2011 eruption of Puyehue-Cordón Caulle, Chile. Figures 3(a) and 4(a) show an ash RGB (red-green-blue) composite image for the eruptions of Eyjafjallajökull and Puyehue-Cordón respectively. This displays a qualitative detection of volcanic ash, with ash ranging in colour from red to yellow, desert dust in magenta and ice particles in black. Table 3 gives the losses for the following examples, where ℓ_{21} is given in the following sections. We assume that in both cases t_j is large enough that the prior probability of ash depends only on $d_j(s_i)$.

4.1. *2010 eruption of Eyjafjallajökull, Iceland*

The April–May 2010 eruption of Eyjafjallajökull in Iceland caused widespread disruption to air traffic lasting several weeks. The 2010 eruption of Eyjafjallajökull was an event where many uncertainties in volcanic ash detection are present in a single satellite image. There were many occasions of simultaneous volcanic ash and desert dust clouds and obscuration of the reverse absorption feature, e.g. due to icing. Here we demonstrate the use of decision theory for hazard detection rather than the suitability of a particular detection scheme. Therefore, although the eruptions was also used for $P(y \mid \text{ash})$, it serves to demonstrate the application well. Figure 3(a) shows an ash RGB composite image from 0615 UTC 8 May 2010. It is possible to see a long volcanic plume extending from Iceland to northern Spain and a Saharan dust cloud to the northeast of the Sahara, blowing over Sicily, Italy. There is also icing of the plume close the volcano. Figures 3(b)–(d) show the pixels classified as contaminated, displayed in yellow with losses $\ell_{21} = 1, 10$ and 100 for Figures 3(b), (c) and (d) respectively. The number of contaminated pixels increases as the loss ℓ_{21} increases. This is most notable around 55°N 20°W, which are likely true positives, and over northern Germany, which may be false positives.

Table 3. Loss table for the examples.

$L(a, x)$	ash	dust	free
a = contaminated	0	1	1
a = uncontaminated	ℓ_{21}	0	0

4.2. *2011 eruption of Puyehue-Cordón Caulle, Chile*

On 4 June 2011 the Puyehue-Cordón Caulle volcanic complex in Chile began to erupt, resulting in the largest eruption of the 21st century so far (Venzke, 2016). The ash composition was substantially different, and therefore spectroscopically different, from the 2010 eruption of Eyjafjallajökull (Gudmundsson *et al.*, 2012; Botto *et al.*, 2013). Figure 4(a) shows an ash RGB image from this eruption at 0700 UTC 7 June 2011, where the ash is mainly displayed in yellow, likely due to its high silica content, with some displayed in magenta to red. Figure 4(b) shows the contaminated pixels in yellow with $\ell_{21} = 2$. The contaminated pixels are mainly consistent between Figures 4(a) and (b) except for some in (b) which are classed as uncontaminated due to thick ice clouds, seen in brown in (a). There are also some speckled contaminated pixels in Figure 4(b) where an ash cloud is not visible in (a).

5. Discussion

Decision theory provides a transparent way to deal with uncertainty in automated procedures which detect atmospheric natural hazards using satellite observations. This allows shared ownership of issuing the hazard between scientists and risk managers, who decide the losses in misidentifying the hazard. This aids authorities in issuing relevant and timely advice, which will lead to safer and more efficient warnings being issued. The losses may be a subjective choice by the risk manager, parametrized by some loss function or decided by the end-user to suit their needs. These losses do not have to be fixed, for example a user could receive a best-case and worst-case scenario based on risk. However, decision theory cannot improve the skill of a detection algorithm; it makes an automated hazard detection scheme better by improving transparency. It is therefore important that the limitations of the detection method are communicated to the risk manager.

The detection method followed in this study is not intended to be globally applicable. Instead it is intended to provide a simple-to-follow application of decision theory to automated detection of atmospheric hazards. However it is interesting to discuss the advantages and limitations of using a simple, computationally cheap detection method. In Figures 3(b)–(d) there is a break in the observation of volcanic ash from the volcano vent. This is due to the presence of both volcanic ash and ice, seen in black in Figure 3(a). Here the method would be improved by including a larger number of volcanic states, or a

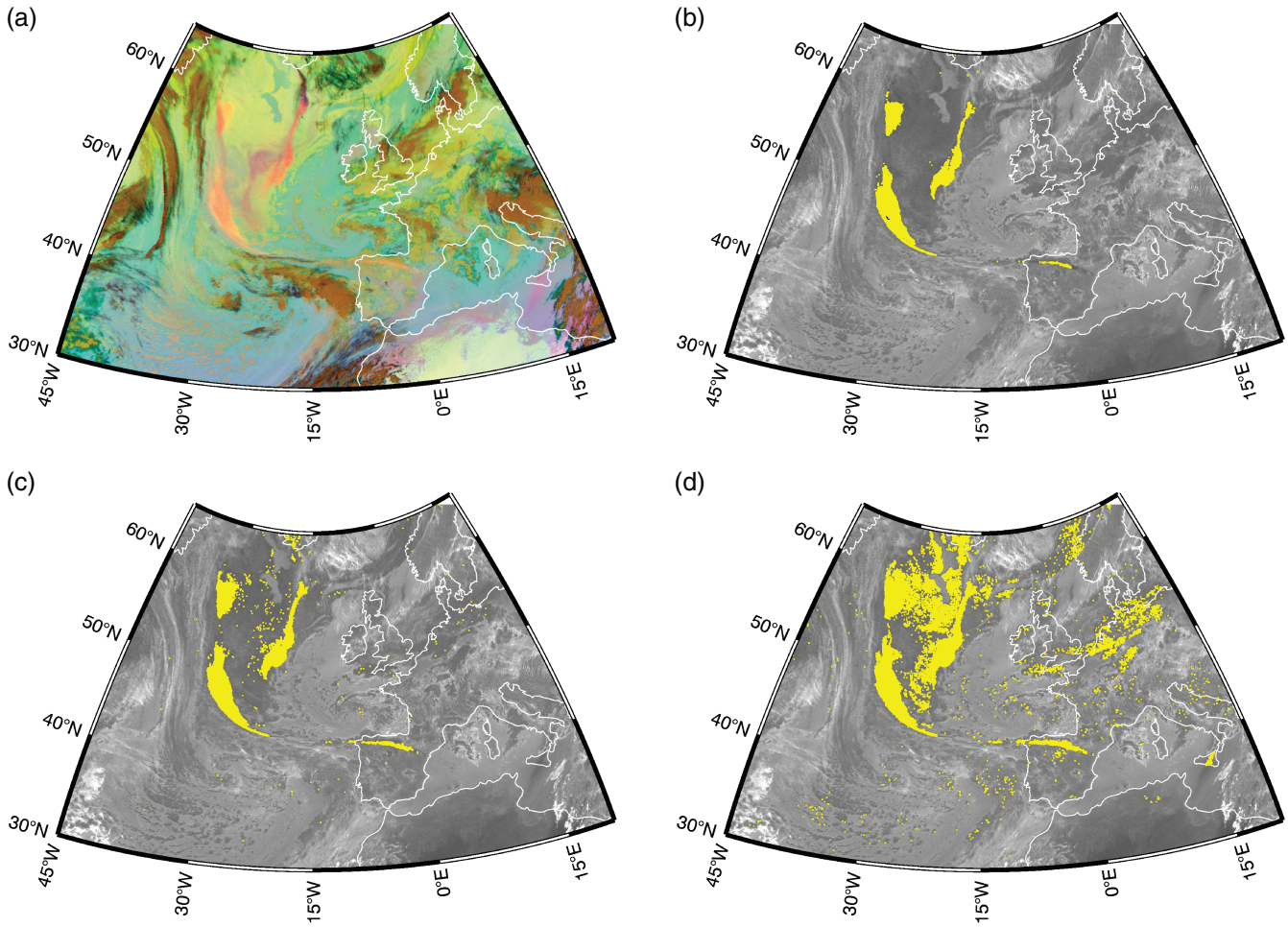

Figure 3. Images from the SEVIRI sensor at 0615 UTC 8 May 2010 during the eruption of Eyjafjallajökull, Iceland. (a) shows an ash RGB image. Contaminated pixels containing volcanic ash are displayed in yellow with: (b) $\ell_{21} = 1$, (c) $\ell_{21} = 10$ and (d) $\ell_{21} = 100$.

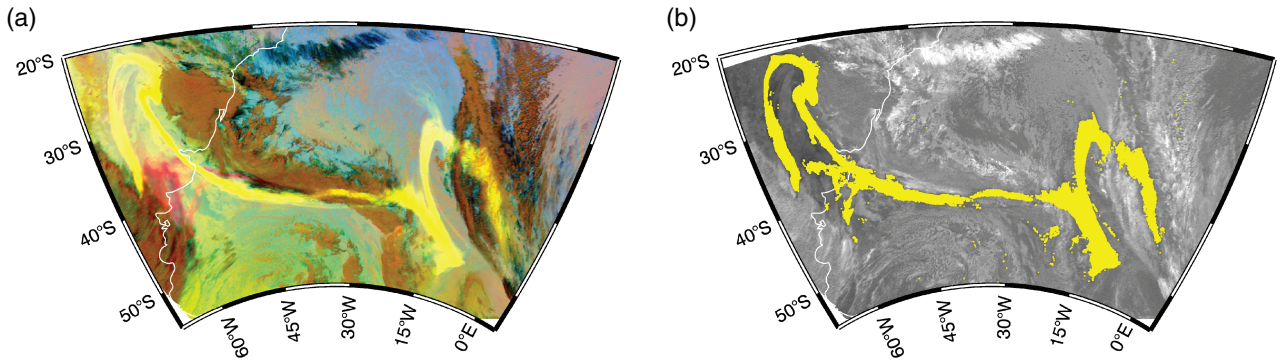

Figure 4. Images from the SEVIRI sensor at 0700 UTC 7 June 2011 during the eruption of Puyehue-Cordón Caulle, Chile. (a) shows an ash RGB image, and (b) contaminated pixels displayed in yellow with $\ell_{21} = 2$.

more complete training set for $P(y \mid \text{ash})$. Figure 3 shows that the sensitivity of the algorithm is higher with a higher loss for ℓ_{21}, for example a large area of ash around 50°N, 20°W is detected when $\ell_{21} = 100$ but not when $\ell_{21} = 1$ or 10. However, this is at the expense of the specificity of the algorithm. This preference to risk is transparent and open to criticism, which should help improve the detection method. When the loss of a false detection for ash is low, the simple method proposed in this study discerns volcanic ash from desert dust even though both commonly exhibit similar values for y. However, the method is unlikely to be able to discern airborne dust from an arid surface as both exhibit similar values for y and are likely to be co-located over land. $P(y \mid \text{ash})$ was fitted to observations from the 2010 eruption of Eyjafjallajökull, so it is unsurprising that it is possible to detect the volcanic ash from this event. It is thus promising that the method works well on the 2011 eruption of Puyehue-Cordón Caulle, which differs geographically, temporally and compositionally. The method in this study may struggle to detect smaller, low-lying ash clouds due to the training set for the observation likelihood. To improve this, different types of ash cloud could have their own state or a larger training set could be used. A more spectrally robust probabilistic algorithm or more rigorous prior probabilities would likely improve both the sensitivity and specificity of the method. The prior probability for volcanic ash relies on knowing that an eruption has occurred, although it is possible to generalize the prior probability using historic data or expertise.

5.1. *Multivariate spatial analysis*

A major limitation in the example method is that it makes decisions on a pixel-by-pixel basis. The aim of an automated hazard warning scheme is to replicate the capabilities of human interpretation, which analyse an image as a whole. Continuing with the

example of volcanic ash, this section suggests how a multivariate spatial detection scheme may benefit from using decision theory.

Under the assumption that there is information that an eruption has occurred, as in the example in this study, a probabilistic forecast from computer simulation (e.g. Bursik *et al.* 2012; Denlinger *et al.* 2012; Dare *et al.* 2016) can inform the prior probability across pixels. An ideal forecast would consist of an ensemble of every possible eruption source parameter and ambient meteorological condition. This is impractical so the prior probability must instead use a finite number of ensemble members, which will likely be limited by computation time. After running ten ensemble members where four result in volcanic ash being present at a given location, then it is not sufficient to simply assign a 40% prior probability of volcanic ash. It is more appropriate to use a Bayesian approach and weight each ensemble member by its prior probability (Katz and Ehrendorfer, 2006). This ensemble prediction forms a prior probability considering the spatial dispersion of the ash cloud. A decision theoretical detection of the ash cloud could provide an input into a forecast, without relying on heuristic selection criteria (as in e.g. Wilkins *et al.*, 2016), which would then inform the next step of hazard detection.

Automated human-like spatial analysis of spectral properties could also benefit from using decision theory. For example the spectral detection method in Pavolonis *et al.* (2015a) and its subsequent spatial classification into cloud objects (Pavolonis *et al.*, 2015b) utilize Bayesian probabilities. The selection criteria for the cloud objects from the spectral detection method are heuristic, limiting transparency and adaptability to the varying needs of users. This presents an opportunity to exploit decision theory, with an initial spectral detection scheme transparently increasing sensitivity through its losses to inform the spatial analysis. The spectral detection scheme then provides an input to the spatial analysis, which transparently adjusts the sensitivity and specificity using losses so that the detection is better suited to the end user.

6. Conclusions

We have presented a method to try to improve transparency in satellite-based hazard warning systems using decision theory. We have proposed decision theory as an alternative to heuristics, which are useful operationally when there is not enough data to specify likelihood functions which differ between sensors and even over the lifetime of a sensor in orbit. Decision theory compensates for some of the issues that are inherent in the use of heuristics. It allows uncertain decisions to be made transparently by stating the loss associated with a given action. The transparency in the losses and the underlying detection method means that any hazard warning scheme based on decision theory is open to criticism, and thus improvement. Decision theory does not require perfect likelihood functions, which it mitigates through Bayesian probability and the specification of losses to actions. The example presented in this study demonstrates the success of combining decision theory with a simple detection method, which can even differentiate volcanic ash from desert dust, while maintaining transparency.

This study chooses the optimum action on a pixel-by-pixel basis, yet atmospheric natural hazards generally exhibit a degree of spatial coherence. An improvement would be to use a multivariate spatial analysis (e.g. Pavolonis *et al.*, 2015b; Bedka and Khlopenkov, 2016). The method outlined here is a simple proof-of-concept, but both probability theory and decision theory are extensible to any level of complexity required by the user. It is therefore possible to apply decision theory to any probabilistic remote-sensing method.

Acknowledgements

We thank Michael Cooke and Peter Francis at the UK Met Office for supplying data for the initial training set for volcanic ash and their input. We acknowledge EUMETSAT or the provision of SEVIRI data via the Earth Observation Portal and ECMWF for provision of data from the ECMWF-MACC Reanalysis data. We would like to thank two anonymous reviewers for their comments, which have greatly improved the manuscript. This study was funded by grant reference NE/K007912/1, a NERC Met Office CASE studentship.

Appendix

Fast Fourier transform noise reduction filter

A fast Fourier transform noise reduction filter can be applied as follows. If $\mathbf{A}$ is an m by n array of elements, where 1 indicates a positive detection and 0 indicates no detection, then the power spectrum is found by:

$$\mathbf{P} = |\mathcal{F}(\mathbf{A})|^2 \tag{A1}$$

and then scaled as:

$$\mathbf{P}_0 = \ln\left(\frac{\mathbf{P}}{\max(\mathbf{P})}\right). \tag{A2}$$

A mask is then formed:

$$\mathbf{M} = \begin{cases} 1 & \text{if } \mathbf{P}_0 > \text{threshold}, \\ 0 & \text{otherwise}, \end{cases} \tag{A3}$$

where the threshold is the maximum value at the edge vertices of the array $\mathbf{P}_0$. The mask is applied to the transform of the original array and inverted back into the spatial domain by

$$\mathbf{A}_{\text{new}} = \Re\left\{\mathcal{F}^{-1}(\mathcal{F}(\mathbf{A}) \circ \mathbf{M})\right\}, \tag{A4}$$

where $\Re\{\cdot\}$ indicates the real part of a complex array and the operator $\circ$ denotes element by element multiplication. The resulting array $\mathbf{A}_{\text{new}}$ is the new filtered array where 1 indicates a positive detection and 0 indicates no detection.

This is derived from the Fourier transform noise reduction filter example in the IDL programming language (Exelis Visual Information Solutions, Boulder, Colorado).

References

Ackerman SA. 1997. Remote sensing aerosols using satellite infrared observations. *J. Geophys. Res. Atmos.* **102**: 17069–17079. https://doi.org/10.1029/96JD03066.

Aminou DMA. 2002. 'MSG's SEVIRI instrument'. *ESA Bull.* **111**: 15–17.

Bedka KM, Khlopenkov K. 2016. A probabilistic multispectral pattern recognition method for detection of overshooting cloud tops using passive satellite imager observations. *J. Appl. Meteorol. Climatol.* **55**: 1983–2005.

Bhattacharya D, Ghosh J, Samadhiya N. 2012. Review of geohazard warning systems toward development of a popular usage geohazard warning communication system. *Nat. Hazards Rev.* **13**: 260–271. https://doi.org/10.1061/(ASCE)NH.1527-6996.0000078.

Botto IL, Canafoglia ME, Gazzoli D, González MJ. 2013. Spectroscopic and microscopic characterization of volcanic ash from Puyehue-(Chile) eruption: Preliminary approach for the application in the arsenic removal. *J. Spectrosc.* **2013**: 254517. https://doi.org/10.1155/2013/254517.

Bursik M, Jones M, Carn S, Dean K, Patra A, Pavolonis M, Pitman EB, Singh T, Singla P, Webley P, Bjornsson H, Ripepe M. 2012. Estimation and propagation of volcanic source parameter uncertainty in an ash transport and dispersal model: Application to the Eyjafjallajökull plume of 14–16 April 2010. *Bull. Volcanol.* **74**: 2321–2338.

Dare RA, Smith DH, Naughton MJ. 2016. Ensemble prediction of the dispersion of volcanic ash from the 13 February 2014 eruption of Kelut, Indonesia. *J. Appl. Meteorol. Climatol.* **55**: 61–78.

DeGroot MH. 1970. *Optimal Statistical Decisions*. Republished 2004. Wiley: Hoboken, NJ.

Denlinger RP, Pavolonis M, Sieglaff J. 2012. A robust method to forecast volcanic ash clouds. *J. Geophys. Res. Atmos.* **117**: D13208. https://doi.org/10.1029/2012JD017732.

Dow K, Cutter SL. 1998. Crying wolf: Repeat responses to hurricane evacuation orders. *Coastal Manage.* **26**: 237–252. https://doi.org/10.1080/08920759809362356.

Economou T, Stephenson DB, Rougier JC, Neal RA, Mylne KR. 2016. On the use of Bayesian decision theory for issuing natural hazard warnings. *Proc. R. Soc. London A* **472**: 20160295. https://doi.org/10.1098/rspa.2016.0295.

Epanechnikov VA. 1969. Non-parametric estimation of a multivariate probability density. *Theory Probab. Appl.* **14**: 153–158.

Francis PN, Cooke MC, Saunders RW. 2012. Retrieval of physical properties of volcanic ash using Meteosat: A case study from the 2010 Eyjafjallajökull eruption. *J. Geophys. Res. Atmos.* **117**: D00U09. https://doi.org/10.1029/2011JD016788.

Gudmundsson MT, Thordarson T, Höskuldsson Á, Larsen G, Björnsson H, Prata FJ, Oddsson B, Magnússon E, Högnadóttir T, Petersen GN, Hayward CL, Stevenson JA, Jónsdóttir I. 2012. Ash generation and distribution from the April–May 2010 eruption of Eyjafjallajökull, Iceland. *Sci. Rep.* **2**: 572. https://doi.org/10.1038/srep00572.

Inness A, Baier F, Benedetti A, Bouarar I, Chabrillat S, Clark H, Clerbaux C, Coheur P, Engelen R, Errera Q, Flemming J, George M, Granier C, Hadji-Lazaro J, Huijnen V, Hurtmans D, Jones L, Kaiser J, Kapsomenakis J, Lefever K, Leitao J, Razinger M, Richter A, Schultz MG, Simmons A, Suttie M, Stein O, Thépaut J-J, Thouret V, Vrekoussis M, Zerefos C. 2013. The MACC reanalysis: An 8-year dataset of atmospheric composition. *Atmos. Chem. Phys.* **13**: 4073–4109.

Katz RW, Ehrendorfer M. 2006. Bayesian approach to decision making using ensemble weather forecasts. *Weather and Forecasting* **21**: 220–231. https://doi.org/10.1175/WAF913.1.

Lindley DV. 1985. *Making Decisions* (2nd ed.). Wiley.

Linke C, Möhler O, Veres A, Mohacsi A, Bozóki Z, Szabó G, Schnaiter M. 2006. Optical properties and mineralogical composition of different Saharan mineral dust samples: A laboratory study. *Atmos. Chem. Phys.* **6**: 3315–3323.

Mackie S, Watson M. 2014. Probabilistic detection of volcanic ash using a Bayesian approach. *J. Geophys. Res. Atmos.* **119**: 2409–2428. https://doi.org/10.1002/2013JD021077.

Mecikalski JR, Berendes TA, Feltz WF, Bedka KM, Bedka ST, Murray JJ, Wimmers AJ, Minnis P, Johnson DB, Haggerty J, Bernstein B, Pavolonis M, Williams E. 2007. Aviation applications for satellite-based observations of cloud properties, convection initiation, in-flight icing, turbulence, and volcanic ash. *Bull. Am. Meteorol. Soc.* **88**: 1589–1607.

Pavolonis MJ, Sieglaff J, Cintineo J. 2015a. Spectrally Enhanced Cloud Objects: A generalized framework for automated detection of volcanic ash and dust clouds using passive satellite measurements: 1. multispectral analysis. *J. Geophys. Res. Atmos.* **120**: 7813–7841. https://doi.org/10.1002/2014JD022968.

Pavolonis MJ, Sieglaff J, Cintineo J. 2015b. Spectrally enhanced cloud objects: A generalized framework for automated detection of volcanic ash and dust clouds using passive satellite measurements: 2. cloud object analysis and global application. *J. Geophys. Res. Atmos.* **120**: 7842–7870. https://doi.org/10.1002/2014JD022969.

Prata A. 1989a. Infrared radiative transfer calculations for volcanic ash clouds. *Geophys. Res. Lett.* **16**: 1293–1296. https://doi.org/10.1029/GL016i011p01293.

Prata A. 1989b. Observations of volcanic ash clouds in the 10–12 m window using AVHRR/2 data. *Int. J. Remote Sens.* **10**: 751–761.

Prata F, Bluth G, Rose B, Schneider D, Tupper A. 2001. Comments on 'Failures in detecting volcanic ash from a satellite-based technique'. *Remote Sens. Environ.* **78**: 341–346.

Rittel HW, Webber MM. 1973. Dilemmas in a general theory of planning. *Policy Sci.* **4**: 155–169. https://doi.org/10.1007/BF01405730.

Sessions WR, Reid JS, Benedetti A, Colarco PR, da Silva A, Lu S, Sekiyama T, Tanaka T, Baldasano J, Basart S, Brooks ME, Eck TF, Iredell M, Hansen JA, Jorba OC, Juang H-MH, Lynch P, Morcrette J-J, Moorthi S, Mulcahy J, Pradhan Y, Razinger M, Sampson CB, Wang J, Westphal DL. 2015. Development towards a global operational aerosol consensus: Basic climatological characteristics of the International Cooperative for Aerosol Prediction Multi-Model Ensemble (ICAP-MME). *Atmos. Chem. Phys.* **15**: 335–362.

Simpson JJ, Hufford G, Pieri D, Berg J. 2000. Failures in detecting volcanic ash from a satellite-based technique. *Remote Sens. Environ.* **72**: 191–217.

Venzke, E (ed.) 2013. *Global Volcanism Program, Volcanoes of the World, v. 4.5.0*'. Smithsonian Institution: Washington, DC. http://dx.doi.org/10.5479/si.GVP.VOTW4-2013 (accessed 26 September 2016).

Wilkins K, Western L, Watson I. 2016. Simulating atmospheric transport of the 2011 Grmsvötn ash cloud using a data insertion update scheme. *Atmos. Environ.* **141**: 48–59.

WMO. 2016. 'Volcanic ash algorithm intercomparison (SCOPE-nowcasting PP2)'. IPET-SUP-2/Doc. 7.1.2. World Meteorological Organization: Geneva, Switzerland.